

# Fine liquid-core polymer fibers for microhydraulic applications: A versatile process design

Rudolf Hufenus<sup>a,\*</sup>, Jonas Hofmann<sup>b,c</sup>, Ali Gooneie<sup>a,d,\*</sup>

<sup>a</sup> Empa, Swiss Federal Laboratories for Materials Science and Technology, Laboratory of Advanced Fibers, Lerchenfeldstrasse 5, 9014 St Gallen, Switzerland

<sup>b</sup> Angst+Pfister Group, Thurgauerstrasse 66, 8052 Zurich, Switzerland

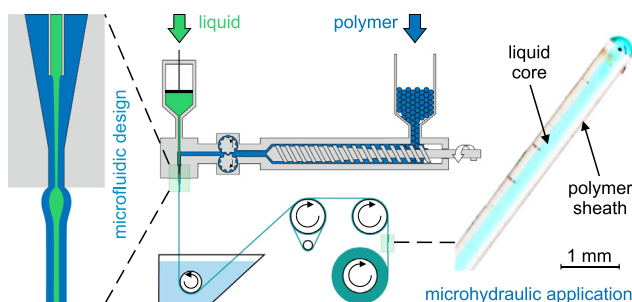
<sup>c</sup> IMES, Institute of Mechanical Systems, Zurich University of Applied Sciences, Technikumstrasse 9, 8401 Winterthur, Switzerland

<sup>d</sup> Circular Plastics, Department of Circular Chemical Engineering, Faculty of Science and Engineering, Maastricht University, Urmonderbaan 22, 6162 AL Geleen, The Netherlands

## HIGHLIGHTS

- A liquid core is continuously fed into a microscale polymer fiber during melt-spinning.
- Different liquid-polymer combinations can be developed by the unique co-extrusion process.
- Computational fluid dynamics calculations confirm the versatility of the process for a wide range of microfluidic conditions.
- Liquid-core fibers show impressive pressure transfer properties, promising for microhydraulic applications.

## GRAPHICAL ABSTRACT



## ARTICLE INFO

### Article history:

Received 24 June 2022

Revised 1 August 2022

Accepted 18 August 2022

Available online 23 August 2022

### Keywords:

Polymer fiber

Melt-spinning

Pressure transfer

Microfluidics

## ABSTRACT

Miniaturization is an essential requirement to advance areas where conventional mechatronic systems may struggle. Microhydraulic devices that combine resilience and compliance could thus revolutionize microrobot applications like locomotion and manipulation. Spurred by the deformability and structural stability provided by veins in insect wings, microscale liquid-core fibers were created, comprising of a polymeric sheath and a liquid core. A microfluidic co-extrusion spinneret was designed, assisted by computational fluid dynamics studies, to achieve such unique liquid-core fibers. Hydraulic pressure transfer tests were successfully applied on fine, up to 10 m long, oil-filled polyamide fibers. The results showed a pressure transfer with a fiber length-dependent delay of  $\sim 20$ – $100$  s for fiber lengths of  $\sim 1$ – $10$  m, and a viscoelastic behavior with relaxation times that behave linearly with fiber length. These findings enable the development of resilient and deformable microhydraulic systems within restricted available space, predestined for applications in soft robotics.

© 2022 The Authors. Published by Elsevier Ltd. This is an open access article under the CC BY license (<http://creativecommons.org/licenses/by/4.0/>).

\* Corresponding authors at: Empa, Swiss Federal Laboratories for Materials Science and Technology, Laboratory of Advanced Fibers, Lerchenfeldstrasse 5, 9014 St Gallen, Switzerland.

E-mail addresses: [rudolf.hufenus@empa.ch](mailto:rudolf.hufenus@empa.ch) (R. Hufenus), [jonas.hofmann@zhaw.ch](mailto:jonas.hofmann@zhaw.ch) (J. Hofmann), [ali.gooneie@maastrichtuniversity.nl](mailto:ali.gooneie@maastrichtuniversity.nl) (A. Gooneie).

<https://doi.org/10.1016/j.matdes.2022.111077>

0264-1275/© 2022 The Authors. Published by Elsevier Ltd.

This is an open access article under the CC BY license (<http://creativecommons.org/licenses/by/4.0/>).

## 1. Introduction

Microhydraulic devices are used in a wide range of applications including medical equipment, robotics, and aerospace instruments [1]. Microsystems for locomotion (e.g., micro air vehicles) and manipulation (e.g., minimally invasive surgery), require sensors and actuators with very small dimensions, simple design and high

reliability [2–4]. While advanced micro-processors and micro-sensors are readily available [5,6], micro-actuators are still a major challenge in designing miniature robots, due to unavailability of suitable components [7]. Hydraulic micro-actuators, which are mainly popular in microfluidic systems, deliver among the highest force densities at microscale, especially in the case of piston actuators [8]. Although less common than electromechanical systems, fluidic pressure-driven soft micro-actuators are gaining attention [9,10].

It is often critical that microhydraulic structures show certain levels of flexibility, for instance in emerging technology of soft robotics, that aims at increasing flexibility and compliance of robots intended for delicate tasks or high maneuverability for robust locomotion [11–14]. Insect wings provide an exemplary bioinspired strategy for designing microsystems by utilizing fine and flexible, liquid-core tubular structures [15]. Beetles have specialized veins that enable seemingly conflicting functions of both wing deformability and structural stability, required for wing storage and flying, respectively [16,17]. Sun et al. [18,19] showed that hemolymph fluid pressure in beetles' veins, built up in the thoracic muscles, facilitates the extension of hind wings during unfolding. This spreading effect is the combined result of hemolymph pressure changes in the veins and the elasticity of the wing structures [20]. Despite these inspiring examples, a robust production strategy to create such soft structures is still missing. Moreover, such a strategy should act synergistically with material design to fulfill deformability and stability requirements.

While research and development mainly concentrate on the actuators themselves [8,21], which can be compared to the insects' thoracic muscles generating hemolymph pressure [22], the role of pressure transmitters (hydraulic hose in macroscale), the respective insect equivalents of space-saving hydrostatic veins [22], apparently is neglected. In soft robotics, flexible structures with embedded fluid channels deform in a predefined way when the fluid is pressurized [21,23–25]. Here, fine elastic and pressure-resistant liquid-core fibers (LCFs) could overcome design constraints in the fabrication of such soft robots, since fluidic pathways can easily be integrated, and powerful pumps could operate externally.

Melt-spinning is the fastest and most economical of all fiber-making processes, yielding elastic fibers as fine as 10  $\mu\text{m}$  in diameter [26]. Based on the principle of bicomponent melt-spinning [27], a special co-extrusion line that enables the pilot-scale production of liquid-filled polymeric fibers was designed [28]. Thus far, it has only ever been possible to fill hollow fibers of limited length in a complex multistep process [29–33]. The ability to produce a continuous LCF is attractive since post-filling of a fine hollow fiber would become increasingly slow and uneconomic at extended lengths [34,35]. The Hagen-Poiseuille law [36] predicts that a hollow fiber of 5  $\mu\text{m}$  core diameter and just 1 m length would take over one month for post-filling with oil (dynamic viscosity of 0.25 Pa·s) at 1-bar. With this unique co-extrusion process, 1000 m of an oil-filled polymeric fiber can be produced in less than a minute. Therefore, melt-spinning of LCFs offers a promising potential to develop fine and flexible microhydraulic structures.

In this study, an extremely versatile microfluidic extrusion process that can be used to create a wide range of LCFs from different polymer-liquid combinations has been designed. A suitable liquid for the core has to meet several requirements to enable continuous and stable injection into polymeric fibers [28]: It must exhibit high thermal stability to withstand extrusion temperatures, and relatively low vapor pressure (<1 atm) at the processing temperature of the polymer sheath. In addition, viscosity ratio and interfacial tension between liquid and polymer must not lead to co-extrusion instabilities. The thermoplastic sheath polymer, on the other hand, mainly requires a high enough melt-strength to enable fiber forming. Polymers suitable for melt-spinning usually show excellent flexibility and stability, and combined with a low viscosity fluid for unhindered pressure transfer, they are viable candidates for fine microhydraulic fibers.

Although this unique process can yield LCFs as fine as  $\sim 50 \mu\text{m}$  in outer diameter, as shown earlier [34], in this study the focus lies on the production of LCFs with outer diameters ranging between  $\sim 250\text{--}850 \mu\text{m}$ , since those allow for easier manipulation in the desired research applications. Nevertheless, the findings will also apply for finer fibers, thus enabling the development of soft microhydraulic actuators.

## 2. Experimental details

### 2.1. Materials

For this study, four different liquids with diverse properties were chosen, as listed in Table 1. The polymer polyethylene glycol (PEG) was of interest because of its high vapor pressure and due to the similarity to bicomponent melt-spinning, where both components are thermoplastic polymers. With the idea of microhydraulic applications, a complex ester oil has been chosen as a representative of hydraulic fluids. Water, the most common liquid, has several exclusive properties [37], which makes it another interesting candidate as core of an LCF. However, due to the low viscosity of water, 5 wt% gelatin had to be added to enable processability. Finally, glycerol has been chosen because it is an abundant, non-toxic viscous liquid with low vapor pressure and low thermal expansion.

Table 2 lists the polymers used to produce LCFs. Polypropylene (PP) and linear low-density polyethylene (LLDPE) are flexible, easy-to-process polymers abundantly utilized for melt-spinning fibers. Cycloolefin polymer (COP) and terpolymer of tetrafluoroethylene, hexafluoropropylene, and vinylidene fluoride (THVP) are transparent polymers suitable to produce polymer optical fibers [39]. Polyolefin plastomer (POP) has been considered because it is a thermoplastic polymer which is highly elastic (tensile elongation at break of 850 % [40]). Polycaprolactone (PCL) is of interest due to its low melting point (Table 2), but also due to its good spinnability and suitability for biomedical applications [41]. Finally, the low-melting-point polyamide copolymer (CoPA) and the high-melting-point polyamide 6 (PA6), have been chosen because polyamides possess outstanding abrasion resistance and high tenacity.

**Table 1**  
Liquids used to produce LCFs. The viscosity at room temperature (23 °C) has been determined applying the standard DIN 53211 [38].

Core liquid	Product name	Provider	Viscosity @ 23 °C (cSt)
PEG 500	Polyethylene glycol 500 Da	Sigma-Aldrich (Buchs, Switzerland)	60
Ester oil	Complex ester Synative ES 3345	Lehmann & Voss & Co. (Hamburg, Germany)	265
Gelatin solution	5 wt% aqueous gelatin solution	Sigma-Aldrich (Buchs, Switzerland)	<50
Glycerol	Glycerol G9012	Sigma-Aldrich (Buchs, Switzerland)	>500

**Table 2**

Polymers used to produce LCFs. The melting temperature,  $T_m$ , is provided by the manufacturer. In the case of THVP, it is taken from a previous publication [42]. COP is an amorphous polymer, with a glass transition temperature,  $T_g$ , of 102 °C [42].

Sheath polymer	Product name	Provider	$T_m$ (°C)
PP-1	Random PP copolymer 621P	Sabic Europe	145
PP-2	Braskem PP homopolymer HSP165G	(Sittard, The Netherlands) Braskem Europe	155
LLDPE	Dowlex SC 2107G	(Weena, The Netherlands) Dow Chemical	250
COP	Zeonor 1020R	(Midland, MI, USA) Zeon Europe GmbH	amorphous
THVP	THVP 2030GZ	(Düsseldorf, Germany) 3 M Deutschland GmbH	130
POP	Versify 4200	(Seefeld, Germany) Dow Chemical	84
PCL	CAPA 6500	(Midland, MI, USA) Perstorp Holding AB.	58
CoPA	Polyamide 6/12 copolymer Grilon CF 6 S	(Malmö, Sweden) EMS-CHEMIE	130
PA6	Grilon A26	(Domat/Ems, Switzerland) EMS-CHEMIE	222
		(Domat/Ems, Switzerland)	

## 2.2. Processing of materials

Melt-spinning, in short requiring an extruder, a spin pack and a fiber draw-down unit, was the method of choice to produce LCFs in a continuous way, as schematically shown in Fig. 1. Dried polymer granulate was fed from a hopper, then melt-extruded and pumped into the spin pack, where a capillary injector, connected to a high-

pressure liquid pump, forced a liquid into the pressurized polymer melt just before the die exit. The melt strand with liquid core was subsequently quenched in a water bath and finally stretched between heated rollers (godets) and wound on a bobbin. More details about the process can be found in a previous publication [26].

Polymer extrusion was carried out on a 19 mm, 25 L/D single screw extruder (Rheomex OS, Thermo Fisher Scientific, Germany). The tip of the injector (Fig. 1c) consists of a capillary tube with inner diameter of 0.7 mm and outer diameter of 1.1 mm. The diameter of the spinneret capillary,  $D_{\text{capillary}}$ , was chosen as 1.5 mm for all spinning trials. Processing temperatures and pressures, melt pump throughput, die exit to quenching water distance, number, temperatures and rotating speeds of the godets, as well as winding speed, were adapted to the respective polymer properties [26]. The draw-down ratio (DDR), i.e. the ratio between winding speed,  $v_w$ , and die exit velocity,  $v_0$ , have been estimated from melt throughput,  $T_p$  (polymer), syringe pump throughput,  $T_l$  (liquid), and  $D_{\text{capillary}}$  as follows:

$$\text{DDR} = \frac{v_w}{v_0} \quad (1)$$

$$v_0 = \frac{4(T_p + T_l)}{\pi D_{\text{capillary}}^2} \quad (2)$$

Assuming a round fiber with outer diameter,  $D_{\text{fiber}}$ , DDR can also be calculated as follows:

$$\text{DDR} = \frac{D_{\text{capillary}}^2}{D_{\text{filament}}^2} \quad (3)$$

## 2.3. Physical properties

To study the fiber cross-section, the LCFs have been embedded within fine cellulose fibers before cutting and examination. Optical microscopy pictures were taken using a VHX-1000 (Keyence, Mecheln, Belgium) system. Scanning electron microscopy (SEM) was conducted on a Hitachi S-4800 SEM (Hitachi High-Technologies, Krefeld, Germany). As prepared, the fiber samples were coated with Au/Pd (5 nm) prior to analysis.

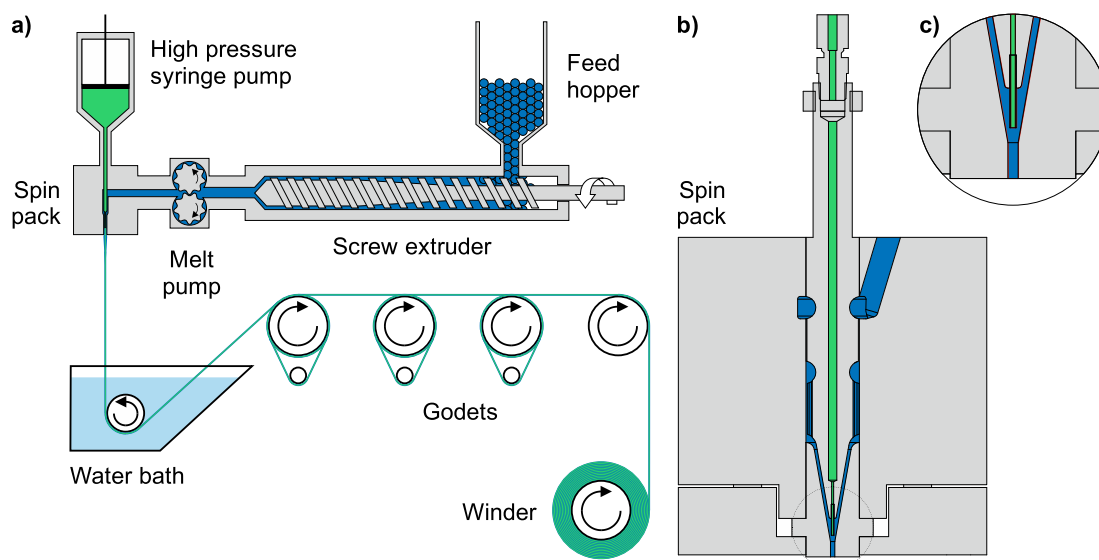


**Fig. 1.** (a) Schematic drawing of the LCF coextrusion spinline with screw extruder, water quenching and fiber take-up unit. (b) Mechanical drawing of the custom-made LCF spin pack. By way of illustration, core liquid and sheath polymer are represented in green and blue, respectively. (c) Blow-up of the LCF co-flow spinneret.

Mechanical testing of the fibers was performed with the tensile testing machine ZwickRoell Retroline Z100 (ZwickRoell, Ulm, Germany). Load-strain curves were determined in reference to the standard ASTM D 2256. Fiber tests were performed with a gauge length of 50 mm using a constant rate of extension of 100 mm/min. Ultimate elastic strength (in N) and ultimate elastic strain (in percentage of the initial gauge length) were obtained by averaging over five measurements.

## 2.4. Pressure transfer test

In order to prove the feasibility of LCF #9 (Table 4) to act as microhydraulic pressure transmitter, a test setup consisting of two identical, custom-made syringes and an in-between, single LCF of defined length was prepared. The custom-made syringes (Fig. 2a) comprise a cylindrical piston of 7 mm diameter within a tightly fitting acrylic glass tube (barrel). The piston is attached to a screw within a thread connected to the barrel, and thus can be manually screwed in and out in a stepless manner. A 10-bar pressure sensor (AG416-001MG-2-TP, Angst + Pfister, Zurich, Switzerland) is connected to the liquid container of the piston. Both cut open ends of an LCF are fed through the open ends (sealed hollow screws) of the two syringes, and the through-hole for the LCF is sealed with epoxy.

For the pressure transfer test, the LCF were cut to a length of  $\sim 1$ –10 m, and each cut fiber end was thread through the epoxy-filled hole of a hollow screw. After curing of the epoxy, the protruding fiber ends (Fig. 2b) were cut with a scalpel to expose the liquid core. The custom-made syringes were filled with ester oil (Table 1) to match the liquid of the fiber core. Lumogen Red 305 (BASF SE, Ludwigshafen am Rhein, Germany) was added to the liquid in a concentration of 0.1 wt% to enhance visibility. The fiber holders were screwed into the syringes with PTFE sealing rings. All the while great care was taken to avoid air inclusions in the liquid.

The two thus prepared syringes (actuator and receiver) with in-between LCF ( $\sim 1$ –10 m) were initially pressurized up to 2 bar by pushing the piston of the actuator syringe. After pressure equalization, monitoring was started and the actuator pressure was increased and manually maintained at 8 bar. When the pressure of the liquid in the receiver syringe reached 7 bar, the actuator pressure was reduced to 2 bar until the receiver pressure dropped to 3 bar, whereupon the actuator pressure was again increased to 8 bar. This cycle was repeated at least four times.

## 2.5. Simulation details

In this study, a systematic set of simulations was carried out (i) to determine the processing limits for developing LCFs, and (ii) to understand the microfluidic co-flow mechanisms that control the process. To achieve these goals, the co-flow extrusion die geometry from the experiments was used as the basis (see Fig. 3), and some of its characteristic dimensions were varied, i.e. the length of the inner core  $L$  and the diameter of the die (outlet) capillary  $D_{\text{capillary}}$ . Benefitting from geometrical symmetry, a quarter of the 3D die geometry was simulated by the multiphaseInterFoam solver in OpenFOAM v8.0 [43]. This solver employs volume-of-fluid (VOF) method over a discretized domain of finite volumes. VOF couples stresses in two (or more) immiscible fluids by an interpolation of their properties (such as viscosity and density) over a thin layer at the interface [44], and has proven to be effective in microfluidic studies [45].

The effects of processing parameters were studied by systematically changing the inlet flowrates of the polymer sheath and the liquid core, see Table 3 for a comprehensive list of processing and material parameters used in the simulations. The volumetric flowrate ratio was consequently varied between 0.016 and 0.718. It should be noted that this range was designed based on (i) the application requirements of LCFs that must contain a certain minimum amount of the core liquid, and (ii) the processing requirements that must contain a certain minimum amount of the polymer sheath to ensure processability. The inlet flowrates were added to the simulations as constant boundary conditions. This constant flowrates resemble the behavior of injection pumps operating at steady state. In some simulations, a sinusoidal oscillating flowrate was used for the liquid core to mimic the behavior of a fluctuating pump. A fluctuating (diaphragm) pump can deliver a continuous flow of core liquid without interruption for refilling as opposed to the injection pump. Thus, it is industrially appealing provided that the (often fast) fluctuations do not lead to processing instabilities and/or discontinuous core (i.e. dripping behavior). In order to simulate such a configuration, cases were developed with oscillation frequencies of  $f = 700$  and  $1400$  Hz, with the latter value reproducing the fluctuation frequency of the diaphragm pump used for respective experiments.

Material properties that control the microfluidic co-flow behavior were also studied [46]. Particularly, the viscosity ratio of liquid to polymer as well as their interfacial tension were altered. The shear viscosity of the polymer was modeled by using the Cross Power Law model  $\mu_c = \frac{\mu_0}{1 + (m\dot{\gamma})^n}$  with  $\mu_0$ ,  $m$ , and  $n$  set to 273 Pa·s,

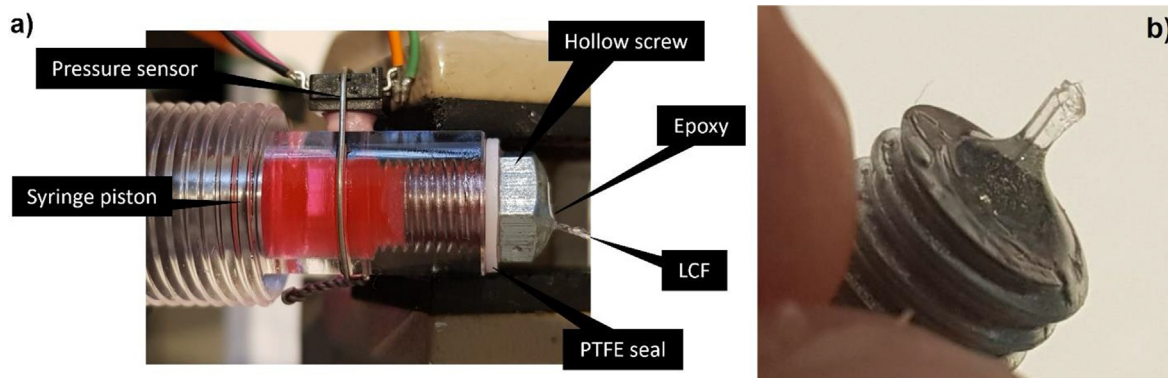


**Fig. 2.** (a) Image of the custom-made syringe, consisting of a piston that precisely fits within a cylindrical barrel, and is additionally sealed with an EPDM O-ring. The open end of an LCF is connected leak-tight to the liquid reservoir within the syringe, and the pressure of the liquid is monitored by an inserted sensor. (b) LCF embedded in epoxy within hollow screw, before cutting to expose the liquid core of the fiber.



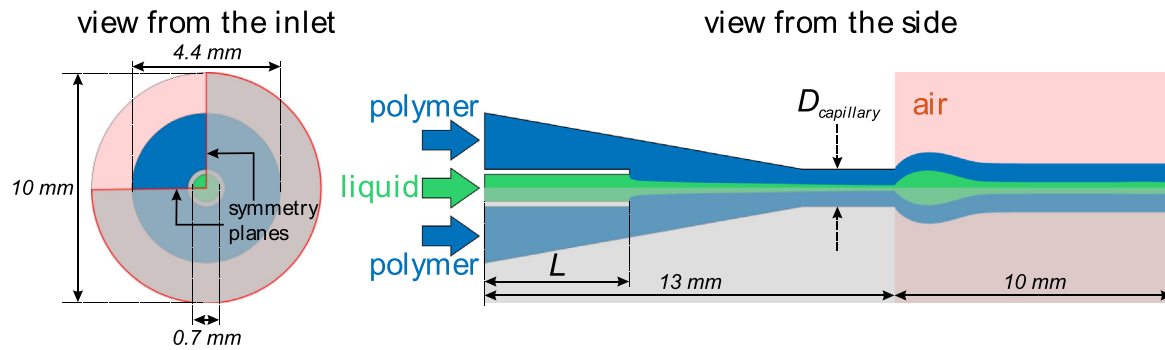


**Fig. 3.** Schematic representation of the simulated co-flow geometry. The die inlet dimensions are shown on the left. The dimensions  $L$  and  $D_{\text{capillary}}$  were varied in different simulations according to Table 3. Co-flow behavior was simulated in a quarter of the geometry by using symmetry conditions (gray areas).

**Table 3**  
Summary of co-flow simulations and their rheological parameters.

Flowrate of polymer sheath $Q_c$ (mm <sup>3</sup> /s)	Flowrate of liquid core $Q_d$ (mm <sup>3</sup> /s)	Flowrate ratio $\frac{Q_d}{Q_c}$	Polymer viscosity $\mu_c$ (Pa·s)	Liquid viscosity $\mu_d$ (Pa·s)	Viscosity ratio $\mu_d/\mu_c$ ( $\times 10^{-5}$ )	Interfacial tension of polymer-liquid $\gamma$ (mN/m)	Observed co-flow behavior
$D_{\text{capillary}} = 1.0$ mm, $L = 1.0$ mm							
9.16	0.44	0.048	27.3	0.0095	34.80	20	stable
9.16	0.44	0.048	27.3	0.0095	34.80	144	dripping flow
9.16	0.44	0.048	27.3	0.0095	3.48	144	stable
9.16	0.44 ( $f = 700$ Hz)	0.048	27.3	0.0095	34.80	20	stable
9.16	0.44 ( $f = 1400$ Hz)	0.048	27.3	0.0095	34.80	20	stable
9.16	0.44 ( $f = 1400$ Hz)	0.048	27.3	0.0095	34.80	144	dripping flow
27.47	0.44	0.016	27.3	0.0095	3.48	144	stable
27.47	0.44	0.016	27.3	0.0095	34.80	144	stable
27.47	6.58	0.239	27.3	0.0095	3.48	144	core expansion
$D_{\text{capillary}} = 1.0$ mm, $L = 6.0$ mm							
9.16	0.44	0.048	27.3	0.0095	3.48	144	stable
9.16	2.19	0.239	27.3	0.0095	3.48	144	stable
27.47	2.19	0.080	27.3	0.0095	3.48	144	stable
27.47	6.58	0.239	27.3	0.0095	3.48	72	stable
27.47	6.58	0.239	27.3	0.285	104.40	72	stable
27.47	6.58	0.239	27.3	1.9	695.97	72	stable
27.47	6.58	0.239	27.3	9.5	3479.85	72	stable
27.47	6.58	0.239	27.3	0.0095	3.48	144	stable
27.47	6.58 ( $f = 1400$ Hz)	0.239	27.3	0.0095	3.48	72	stable
$D_{\text{capillary}} = 1.0$ mm, $L = 9.0$ mm							
9.16	0.44	0.048	27.3	0.0095	3.48	144	stable
9.16	0.44 ( $f = 1400$ Hz)	0.048	27.3	0.0095	3.48	144	stable
27.47	0.44	0.016	27.3	0.0095	3.48	144	stable
$D_{\text{capillary}} = 1.5$ mm, $L = 6.0$ mm							
9.16	6.58	0.718	27.3	0.0095	3.48	72	core expansion
9.16	6.58	0.718	27.3	0.285	104.40	72	stable
9.16	6.58	0.718	27.3	1.9	695.97	72	stable
9.16	6.58 ( $f = 700$ Hz)	0.718	27.3	0.0095	3.48	72	core expansion
9.16	6.58 ( $f = 1400$ Hz)	0.718	27.3	0.0095	3.48	72	core expansion
27.47	6.58	0.239	27.3	0.0095	3.48	72	stable
27.47	6.58	0.239	27.3	0.285	104.40	72	stable
27.47	6.58	0.239	27.3	1.9	695.97	72	stable
27.47	6.58 ( $f = 700$ Hz)	0.239	27.3	0.0095	3.48	72	stable
27.47	6.58 ( $f = 1400$ Hz)	0.239	27.3	0.0095	3.48	72	stable

$0.001 \text{ s}^{-1}$ , and 0.5, respectively. These parameters represent the typical flow behavior of common polymers used in melt extrusion and spinning [47–49]. In some simulations,  $\mu_0$  was set to 27.3 Pa·s in order to investigate the co-flow behavior when the sheath polymer has a lower melt viscosity than commonly encountered in industrial production. The liquid core was modeled as a Newtonian fluid with a constant viscosity,  $\mu_d$ , in the range of 0.0095–9.5 Pa·s, which corresponds to the typical viscosities of fluids used as the core in the melt-spinning process (Table 1). Consequently, their viscosity ratio was varied between  $3.48 \times 10^{-5}$ – $3.48 \times 10^{-2}$  cover-

ing three decades. Air was modeled as a Newtonian fluid with a constant viscosity of  $1.48 \times 10^{-5}$  Pa·s. The densities of polymer, liquid, and air were set to 910, 950, and  $1 \text{ kg/m}^3$ , respectively.

The interfacial tension,  $\gamma$ , between polymer and liquid was varied between 20 and 144 mN/m to study the effects of this critical parameter on the co-flow behavior. It is well known that high  $\gamma$  can promote breakup of the dispersed phase and lead to dripping behavior [46]. Thus, this wide range of  $\gamma$  allows to examine the flexibility of the co-flow process in extreme cases. Finally, the interfacial tensions of polymer–air and liquid–air interfaces were

**Table 4**

LCFs produced in this study. Core ratios are estimated from  $T_i$  and  $T_p$ , and DDR from Equations (1) and (2); core and fiber diameters were taken from optical microscopy cross-sections (5 measurements), ultimate elastic strength and strain from the load–strain curves (5 measurements).

No.	Sheath polymer	Core liquid	Throughput		Core ratio (vol%)	Winding speed $v_w$ (m/min)	Draw-down ratio DDR	Core diameter ( $\mu\text{m}$ )	Fiber diameter ( $\mu\text{m}$ )	Ultimate elastic strength (N)	Ultimate elastic strain (%)
			liquid $T_i$ (ml/min)	polymer $T_p$ (ml/min)							
1	PP-1	PEG 500	1.4	8.1	15	140	26	112 $\pm$ 6	297 $\pm$ 10	2.1 $\pm$ 0.1	31 $\pm$ 1
2	COP	Glycerol	0.3	6.3	5	120	32	59 $\pm$ 14	267 $\pm$ 40	4.2 $\pm$ 0.2	5.6 $\pm$ 0.1
3	THVP	Glycerol	2.0	6.6	23	45	9	245 $\pm$ 28	497 $\pm$ 21	4.4 $\pm$ 0.7	421 $\pm$ 27
4	PCL	Gelatin solution	1.0	6.0	14	10	3	307 $\pm$ 27	855 $\pm$ 24	4.8 $\pm$ 0.6	4.5 $\pm$ 0.7
5	POP	Ester oil	1.5	6.6	19	60	13	170 $\pm$ 16	408 $\pm$ 19	0.8 $\pm$ 0.1	42 $\pm$ 2
6	PP-2	Ester oil	2.0	6.0	25	100	22	155 $\pm$ 12	319 $\pm$ 26	9.8 $\pm$ 0.6	21 $\pm$ 1
7	LLDPE	Ester oil	2.0	6.0	25	100	22	161 $\pm$ 12	324 $\pm$ 8	7.2 $\pm$ 0.2	21 $\pm$ 1
8	CoPA	Ester oil	1.0	6.6	13	80	19	116 $\pm$ 6	333 $\pm$ 4	26 $\pm$ 1	28 $\pm$ 2
9	PA6	Ester oil	2.5	10.5	19	65	9	221 $\pm$ 6	501 $\pm$ 7	4.4 $\pm$ 0.2	5.3 $\pm$ 0.4

both set to 72 mN/m [50]. Although this value describes the pure water–air interfaces, it was noticed in preliminary simulations that it does not influence the results significantly.

The simulations were initialized by flowing the polymer into the geometry until it reached steady state, which was achieved by simulating  $\sim 1$ –2 s of real time. Afterward, the flow of the liquid core was started until it reached steady state, which was achieved by simulating  $\sim 1$ –4 s of real time. In all cases, the steady state was achieved when the changes in velocity profiles near the die exit (i.e. before entering the air-filled cylinder) and near the geometry exit (i.e. near the end of the air-filled cylinder) became insignificant. These transient simulations were performed by using Euler's method with a maximum time step of 5  $\mu\text{s}$ . The time step was dynamically modified during the simulations to maintain a Courant number smaller than 1.

### 3. Results and discussion

#### 3.1. Microfluidic co-flow behavior

Microfluidic co-flow behavior is controlled by (i) the microfluidic geometry, (ii) the flow parameters, and (iii) the fluid properties [46,51]. These factors can be represented by Capillary number of the outer (continuous) phase,  $Ca_c = \frac{\mu_c U_c}{\gamma}$ , and Weber number of the inner (dispersed) phase,  $We_d = \frac{\rho_d d_d U_d^2}{\gamma}$ , in which  $U_c$  and  $U_d$  are the flow speeds of the continuous and dispersed phases respectively,  $\rho_d$  is the density of the dispersed phase, and  $d_d$  is the characteristic diameter of the dispersed phase. Variations of these numbers lead to different co-flow behaviors including dripping regime, jetting regime, and transition from dripping to jetting [46]. While the dripping behavior results in the formation of dispersed droplets of the inner phase, a continuous thread of the inner phase can be stabilized in the jetting regime by increasing its flow-rate [52]. This latter scenario is particularly interesting for the development of melt-spun LCFs.

$Ca_c$  and  $We_d$  were calculated in all of the simulations to compare their co-flow behavior with the literature, see Fig. 4. Approximate domains of different co-flow regimes in a microfluidic coaxial geometry are added to Fig. 4 from the data compilation published in the review paper by Nunes et al. [46]. Most of the simulated cases, including those that copy the experimental coextrusion conditions applied in this work, fall in the jetting regime and show a stable co-flow for a wide range of material combinations and processing conditions. On the other hand, a few simulation cases with extreme conditions (i.e. unrealistic for industrial coextrusion purposes) fall in the transition regime. These cases all led to dripping behavior as also summarized in Table 3. As a

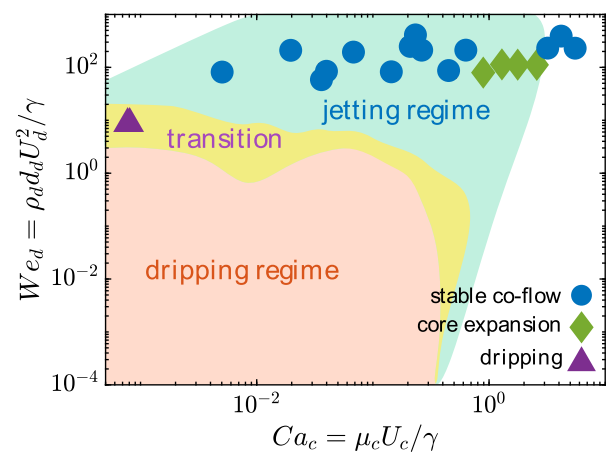


**Fig. 4.**  $Ca_c$  and  $We_d$  calculated from the simulations (markers) compared with the approximate domains of different co-flow regimes from literature (colored areas), see Nunes et al. [46] and the references within.

result, melt-spinning of LCFs is theoretically a versatile approach. This stable co-flow behavior is mainly achieved owing to the fast processing speeds and the high polymer (sheath) viscosity. In comparison with theory, the experimental results also confirm that a continuous liquid core can be injected into a melt-spun polymer fiber in most cases studied.

It should be noted here that an important distinction between theory and practice is the instability of co-flow in the startup phase of the process. In some simulations that fall in the jetting regime, the liquid core shows dimensional instabilities (expansion) due to a sudden pressure release at the die exit, which destabilizes the jetting flow. At this point, the fiber might break and a continuous process may not be achieved. These cases are noted in Table 3. In such simulations, a stable co-flow eventually emerges in steady state. To avoid this problem in experiments, flow of the liquid core was started first, and the sheath polymer was delivered subsequently. In this order, it was possible to initialize a continuous coextrusion process in all cases. In extreme cases, expansion along with large mismatch of core and sheath flowrates can lead to the dripping flow behavior (Fig. 5).

#### 3.2. Production and applicability of liquid-core fibers

In order to prove the versatility of the unique coextrusion process, a variety of thermoplastic polymers with different suitable liquids has been combined. A selection of successfully melt-spun LCFs is presented in Table 4, together with processing parameters

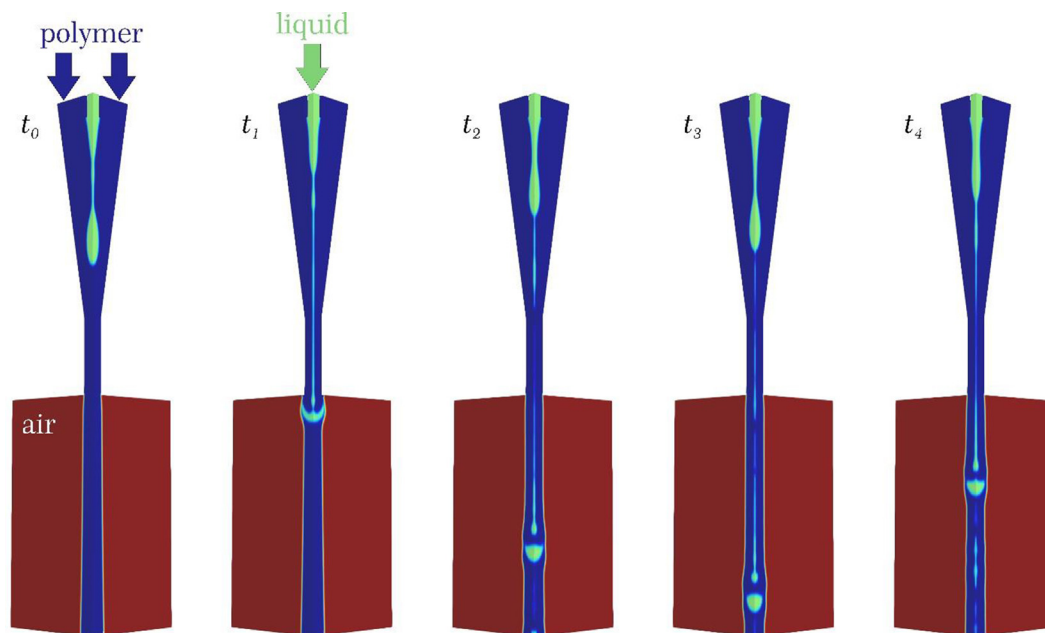


**Fig. 5.** Representative dripping behavior of polymer-liquid co-flow at different times  $t_0$  to  $t_4$ : ( $t_0$ ) start of liquid core flow, ( $t_1$ ) dimensional instability (expansion) of the liquid core, ( $t_2$ - $t_4$ ) dripping flow.

and dimensional properties. However, melt-spinning is a very challenging process with rather narrow processing windows. Processability is further complicated by the injection of a liquid into the polymer melt. In consequence, DDR, which defines the fineness of a fiber at a given throughput, cannot be chosen at will, but has to be evaluated in order to find a stable processing condition. Both, DDR and throughput of core liquid and sheath polymer, need to be within a certain range to prevent spinning instabilities [26]. In addition, depending on the toughness of the sheath polymer, the volume percent of the core liquid cannot exceed a certain value. The highest value ever achieved with this technique so far was 25 vol%.

The required melt-processing temperatures of the polymers ranged from 90 °C (PCL) to 240 °C (PA6), and the resulting spinneret pressures ranged between 38 and 127 bar. In some cases, the resulting core and fiber cross-sections undulate considerably (Table 4), which can be explained by the occurrence of draw resonance, which can result from periodic oscillations of melt velocity, cross-section area and spinline tension [26]. As it has been proven elsewhere [34], much finer liquid-core fibers ( $\varnothing < 50 \mu\text{m}$ ) could be produced at 1000 m a minute when quenching the fiber in air instead of water. However, such fine fibers are much more difficult to manipulate, which is the reason why only LCFs quenched in a water bath have been considered.

Under axial deformation, most unoriented or partially oriented polymer fibers experience a transition from elastic to plastic deformation at the so-called yield point (local maxima) in the load-strain curve [26]. Since deformation is irreversible after passing the yield point, the latter represents ultimate elastic strength and strain (Table 4).

SEM was utilized to illustrate cross-sections of the LCFs produced (Fig. 6). The liquid core has evaporated due to the partial vacuum in the SEM sample chamber, revealing hollow fiber tips (with the exception of LCF #7). The fine membrane in the core of LCF #4 most probably is remaining gelatin after evaporation of water. Eccentricity of the core can be explained by small tolerances in centering of the injector capillary, while out-of-roundness and striations in the sheath stem from cutting of the fibers.

Each LCF presented in Table 4 has unique applications, which will briefly be addressed here. PEG, a non-toxic, organic phase

change material with high latent enthalpy [53], was utilized to prepare a fiber (LCF #1) with phase change properties, where the PP sheath serves as flexible supporting material. The effectiveness of such an approach has been proven elsewhere [54].

Substituting the solid core of a polymer optical fiber (POF) with a transparent liquid yielded luminescent waveguides with improved mechanical robustness [55]. To this end, glycerol, having a refractive index (RI) of 1.47, has been coextruded with COP (RI = 1.53) and THVP (RI = 1.35). Since total internal reflection requires a sheath with lower RI, the glycerol-COP core-sheath fiber (LCF #2) expectedly showed very high attenuation, while the liquid-filled THVP fiber (LCF #3) is a good candidate for highly flexible POFs [55].

For medical applications, in particular for drug delivery systems, a water containing LCF might be of high interest. For this purpose, PCL has been chosen as sheath polymer. Since PCL could be melt-processed at  $\sim 90$  °C, the evaporation of water during coextrusion was prevented. To improve processability, 5 % gelatin has been added to distilled water in order to increase the viscosity of the core liquid (LCF #4).

Microhydraulic applications require a non-compressible, non-corrosive synthetic oil with low vapor pressure and high thermal stability. Therefore, it has been decided to coextrude a complex ester oil (Synative ES 3345, Table 1) with a variety of thermoplastic polymers (Table 2). Polyolefins are excellent sheathing materials since they are lightweight (density  $< 1 \text{ g/cm}^3$ ) and chemically resistant. POP was utilized for melt-spinning an LCF (#5) due to its high extensibility, resulting in extraordinary flexibility of the fiber. PP and LLDPE, on the other hand, yielded polyolefinic LCFs (#6 and #7, respectively) with considerably higher stiffness compared to POP, which prevents bulging when the core liquid is pressurized.

In contrast to polyolefins, the outstanding toughness of polyamides enables applications in harsh conditions. When softness of the sheath is favored, CoPA can be considered (LCF #8), while PA6 is an excellent choice for microhydraulic applications that ask for robustness and reliability (LCF #9). The latter fiber has thus been elected to perform hydraulic tests that prove its respective practicality (Section 3.3).

To exemplarily measure diameter uniformity of LCF #9 during production, the two axis diameter measuring device Zumbach

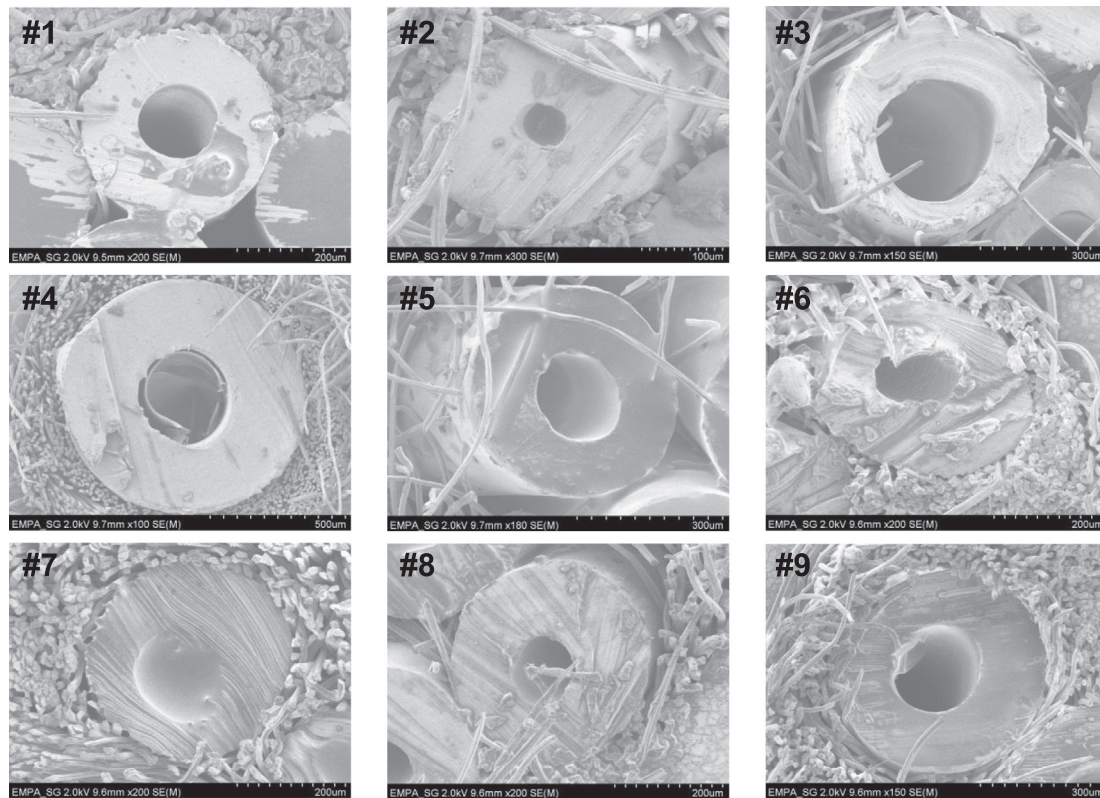


**Fig. 6.** Exemplary SEM cross-section images of all LCFs presented in this study (the fine surrounding fibers have been used for LCF embedding to facilitate cutting). #1: PEG core with PP sheath; #2: glycerol core with COP sheath; #3: glycerol core with THVP sheath; #4: gelatin solution core with PCL sheath; #5: ester oil core with POP sheath; #6: ester oil core with PP sheath; #7: ester oil core with LLDPE sheath; #8: ester oil core with CoPA sheath; #9: ester oil core with PA6 sheath.

ODAC 18XY (Zumbach Electronic AG, Orpund, Switzerland) was installed before the last godet (Fig. 1). As can be seen in Fig. 7, the uniformity of the melt-spun fiber is excellent, with deviations from the mean diameter ranging at  $\sim 1\%$ .

### 3.3. Microhydraulic properties of the selected liquid-core fiber

Microhydraulic properties of the exemplary fiber LCF #9 were tested by a pressure transfer test as described before. In these experiments, the fiber is fixed between two syringes that apply and measure pressure at the two ends of the fibers. Representative

results of such experiments on two fibers with 1.14 and 9.57 m lengths are shown in Fig. 8. In one measurement cycle, the actuator syringe applies a sudden pressure of 8 bars on one end of the fiber and the receiver syringe measures the pressure respond at the other end. After the pressure at the receiver reaches 7 bars, the applied pressure is abruptly reduced to 2 bars and again the pressure relaxation is measured by the receiver syringe. This cycle was repeated at least 3 times for each fiber. At first, it is clear that the response of the fibers to an applied pressure is a reversible process. This is particularly important in certain force-sensing applications that require the fiber to preserve its performance after repeated

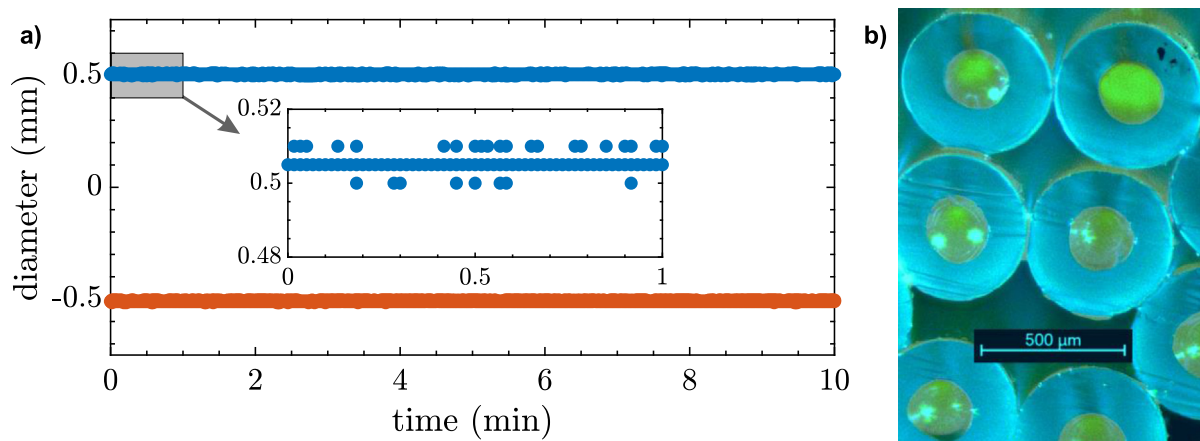


**Fig. 7.** (a) Diameter of LCF #9 measured online during melt-spinning over a period of 10 min. For better visibility, the results of the two axis (X/Y) measurement are plotted as positive (X) and negative (Y) values, respectively. The inset displays a blow-up of the X axis for the first minute. The resolution of the diameter measurement was  $5\ \mu\text{m}$ . (b) Microscopic image depicting cross-sections of a bundle of LCFs #9 (out-of-roundness and striations in the sheath stem from cutting of the fibers).



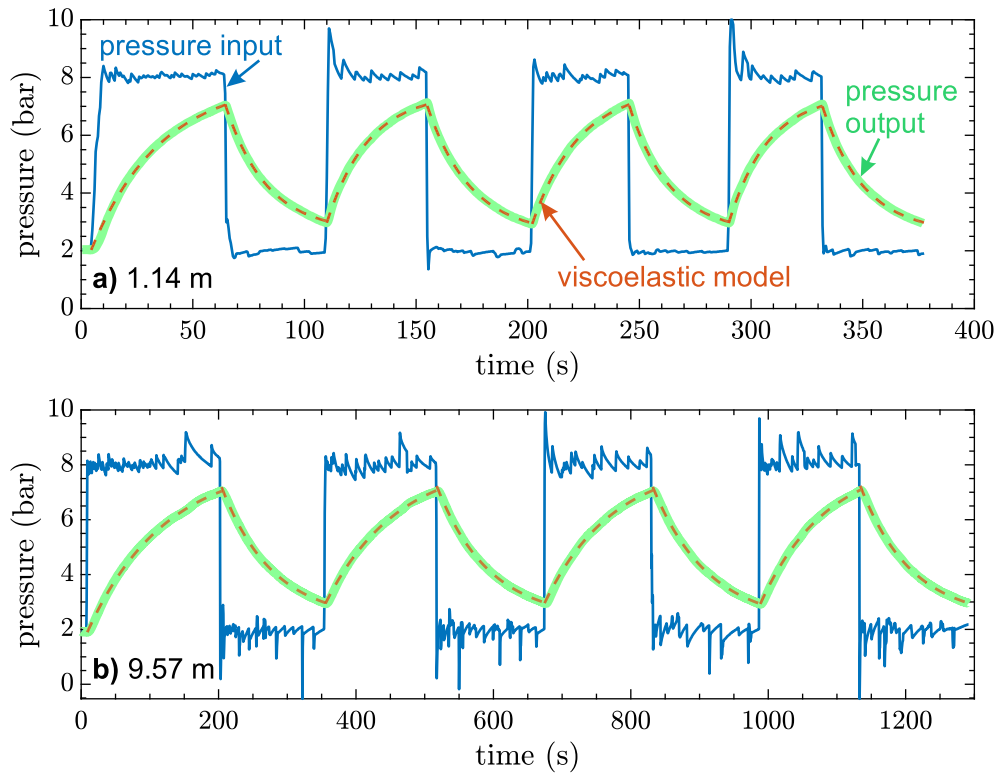


**Fig. 8.** Repeated cycles of input pressure on LCF #9, with a length of (a) 1.14 m and (b) 9.57 m, by the actuator syringe (blue line) and the output pressure read by the receiver syringe (green line). The response of the fiber is modeled by a combination of Kelvin-Voigt (for creep) and Maxwell (for relaxation) viscoelastic models (red dashed line).

actuation cycles. Moreover, the results show that the pressure at the receiver changes gradually over time, which can be described by a simple viscoelastic model. During the high-pressure stage (8 bars), the creeping pressure increase follows a Kelvin-Voigt behavior [56]. The pressure relaxation stage (2 bars), on the other hand, is best described by a Maxwell model [56]. A possible explanation for the gradual change of pressure can be the expansion of the sheath polymer under the internal pressure of the liquid core [57]. This behavior relaxes the pressure buildup along the fiber length and hence results in a respective gradual pressure buildup at the receiver syringe. A similar mechanism affects the pressure relaxation stage.

The average response time of the fibers with varying length (between 1 and 10 m) to actuation were estimated from the relaxation times of the Kelvin-Voigt ( $\tau_K$ ) and Maxwell ( $\tau_M$ ) viscoelastic models, see Table 5 and Fig. 9. The fitted relaxation times both follow a linear behavior with the fiber length. This supports the earlier hypothesis that the elastic stretching of the polymer sheath induced the time-dependent pressure at the receiver syringe. Another interesting observation relates to the offset of the relaxation times at vanishing fiber lengths. Both fitted lines coincide

at an offset relaxation time of.  $\tau = 4.4^{\circ}$ s This offset is ascribed to the response time of the syringes in the pressure transfer setup.

With regard to possible applications, enabling adaptive stiffness control with LCF technology could improve the locomotion capabilities of soft robots in complex environments, for example, (i) in perching on vertical substrates, where tuning body and tail stiffness is critical [58], (ii) in the transition from water to land, where the same robotic limb must function as both a flipper in the water

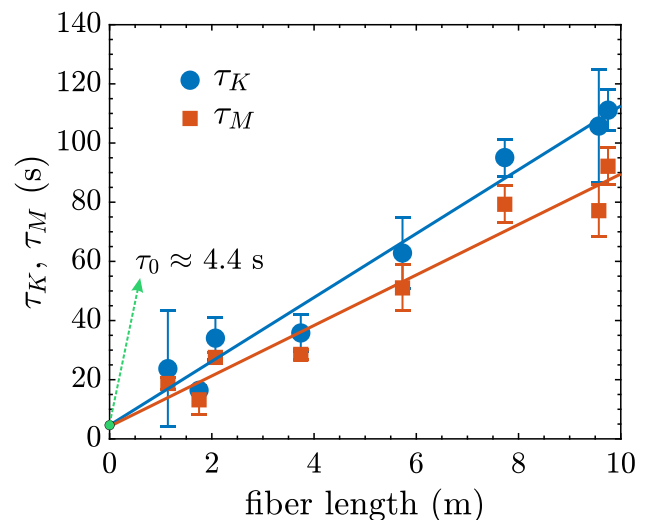


**Fig. 9.** Relaxation times of Kelvin-Voigt ( $\tau_K$ ) and Maxwell ( $\tau_M$ ) models as a function of different lengths of LCF #9. The error bars are calculated from sequential pressure cycles for each fiber and are multiplied by a factor of 5 for better visibility. The lines show the best fits to the data, and their offset is shown by the green marker at.  $\tau_0 = 4.4^{\circ}$ s.

**Table 5**

Relaxation times of Kelvin-Voigt ( $\tau_K$ ) and Maxwell ( $\tau_M$ ) models for different lengths of LCF #9. The errors are calculated from sequential pressure cycles for each fiber.

Length (m)	$\tau_K$ (s)	$\tau_M$ (s)
1.14	$23.7 \pm 3.9$	$18.7 \pm 0.4$
1.75	$16.4 \pm 0.3$	$13.2 \pm 0.9$
2.07	$34.0 \pm 1.4$	$27.5 \pm 0.3$
3.74	$35.8 \pm 1.2$	$28.5 \pm 0.3$
5.73	$62.8 \pm 2.4$	$51.0 \pm 1.5$
7.73	$95.1 \pm 1.2$	$79.3 \pm 1.2$
9.57	$105.7 \pm 3.8$	$77.1 \pm 1.7$
9.75	$111.1 \pm 1.4$	$92.1 \pm 1.2$

and a load bearing leg on land [59], (iii) when traversing over soft substrates or granular media [60], or (iv) during undulatory movements such as swimming (actuating air pressure of 0.8–1.2 bar) [6,24]. Furthermore, the tail is emerging as an important appendage in numerous locomotion modes such as the aforementioned perching [58], but also during object traversal [12] and mid-air reorientation [13,61]. The ability to tune the tail stiffness to the environment would therefore enable a wide variety of different locomotion modes while only adding a single appendage to the robot.

#### 4. Conclusions

Due to capillary resistance, filling fine hollow fibers within reasonable time can only be achieved with fibers of limited length. To overcome this bottleneck, a unique co-extrusion line to produce fine polymeric fibers with a continuous liquid core has been developed. Based on the principle of bicomponent spinning [27], a microfluidic extrusion process to melt-spin kilometer-long LCFs that are filled during production has been designed. The liquid is injected under high pressure through a capillary and meets the molten polymer within a co-flow channel before exiting the spinneret. The resulting fiber can be quenched, drawn and wound like regular melt-spun fibers.

To determine the processing limits of melt-spinning LCFs, a comprehensive set of numeric simulations has been performed. It has been found that with the implemented co-flow spinneret design, the choice of polymer-liquid combinations examined, and the process parameters applied, the process falls in the jetting regime. This co-flow regime, which results from fast processing speeds and high polymer viscosity, assures a continuous, uniform and centered liquid core within a stable polymeric sheath.

An intriguing application aimed for is soft robotics, where pressure-resistant LCFs could form a net of microhydraulic elements, embedded in various forms and shapes with restricted available space, actuated by powerful external pumps. This would be beneficial since LCFs can be embedded in flexible structures that deform in a predefined way when the fluid is pressurized. In order to prove the feasibility of the LCFs for force transmission in microhydraulics, pressure transfer tests on different lengths (up to 10 m) of an exemplary oil-filled polyamide fiber have been applied. The results show that co-extruded, melt-spun LCFs can transmit forces over extended lengths in a reversible and reliable way, and thus have the potential to refine microhydraulic structures. Further tests mimicking specific applications in soft robotics are suggested. Pressure range, fiber and size of the pump's reservoir are key parameters influencing the pressure transmitter's characteristics.

#### CRediT authorship contribution statement

**Rudolf Hufenus:** Conceptualization, Methodology, Formal analysis, Investigation, Writing – original draft, Writing – review & editing, Visualization, Supervision, Project administration, Funding acquisition. **Jonas Hofmann:** Methodology, Investigation, Writing – review & editing, Visualization. **Ali Gooneie:** Conceptualization, Methodology, Formal analysis, Investigation, Writing – original draft, Writing – review & editing, Visualization, Supervision, Funding acquisition.

#### Data availability

The raw and processed data required to reproduce these findings cannot be shared at this time as the data also forms part of an ongoing study.

#### Declaration of Competing Interest

The authors declare that they have no known competing financial interests or personal relationships that could have appeared to influence the work reported in this paper.

#### Acknowledgments

The authors acknowledge the support of Mathias Lienhard, Figen Selli, Konrad Jakubowski and Benno Wüst in the melt-spinning experiments, Sandro Lehner in the viscosity measurements, Patrick Rupper in optical and SEM characterization, Markus Hilber in spinneret design, sample preparation and mechanical characterization, and Ardian Jusufi for insightful discussions. This research was partially funded by Innosuisse (Switzerland), grant number 49822.1 IP-ENG.

#### References

- [1] A. Konda, D. Lee, T. You, X. Wang, S. Ryu, S.A. Morin, Reversible Mechanical Deformations of Soft Microchannel Networks for Sensing in Soft Robotic Systems, *Advanced Intelligent Systems* 1 (4) (2019) 1900027, <https://doi.org/10.1002/aisy.201900027>.
- [2] S. Fatikow, U. Rembold, *Microsystem Technology and Microrobotics*, Springer, Berlin Heidelberg, 1997.
- [3] T. Ranzani, S. Russo, F. Schwab, C.J. Walsh, R.J. Wood, Deployable stabilization mechanisms for endoscopic procedures, in: 2017 IEEE International Conference on Robotics and Automation (ICRA), 2017. pp. 1125–1131.
- [4] X. Zhu, Y. Hu, G. Wu, W. Chen, N. Bao, Two-Dimensional Nanosheets-Based Soft Electro-Chemo-Mechanical Actuators: Recent Advances in Design, Construction, and Applications, *ACS Nano* 15 (6) (2021) 9273–9298.
- [5] S. Xu, D.M. Vogt, W.-H. Hsu, J. Osborne, T. Walsh, J.R. Foster, S.K. Sullivan, V.C. Smith, A.W. Rousing, E.C. Goldfield, R.J. Wood, Biocompatible Soft Fluidic Strain and Force Sensors for Wearable Devices, *Adv. Funct. Mater.* 29 (7) (2019) 1807058, <https://doi.org/10.1002/adfm.201807058>.
- [6] B. Wright, D.M. Vogt, R.J. Wood, A. Jusufi, Soft Sensors for Curvature Estimation under Water in a Soft Robotic Fish, in: 2019 2nd IEEE International Conference on Soft Robotics (RoboSoft), 2019. pp. 367–371.
- [7] G. Caprari, T. Estier, R. Siegwart, Fascination of Down Scaling – Alice the Sugar Cube Robot. IEEE International Conference on Robotics and Automation (ICRA). San Francisco, CA, USA, 2000.
- [8] M. De Volder, D. Reynaerts, Pneumatic and hydraulic microactuators: a review, *J. Micromech. Microeng.* 20 (4) (2010) 043001, <https://doi.org/10.1088/0960-1317/20/4/043001>.
- [9] L. Hines, K. Petersen, G.Z. Lum, M. Sitti, Soft Actuators for Small-Scale Robotics, *Adv. Mater.* 29 (13) (2017) 1603483, <https://doi.org/10.1002/adma.201603483>.
- [10] R.Z. Gao, C.L. Ren, Synergizing microfluidics with soft robotics: A perspective on miniaturization and future directions, *Biomicrofluidics* 15 (1) (2021) 011302, <https://doi.org/10.1063/5.0036991>.
- [11] R. Siddall, G. Byrnes, R.J. Full, A. Jusufi, Tails stabilize landing of gliding geckos crashing head-first into tree trunks, *Communications Biology* 4 (1) (2021) 1020.
- [12] R. Siddall, T. Fukushima, D. Bardhi, B. Perteshoni, A. Morina, E. Hasimja, Y. Dujaka, G. Haziri, L. Martin, H. Banerjee, A. Jusufi, Compliance, mass distribution and contact forces in cursorial and scansorial locomotion with biorobotic physical models, *Adv. Rob.* 35 (7) (2021) 437–449.
- [13] T. Fukushima, R. Siddall, F. Schwab, S.L.D. Toussaint, G. Byrnes, J.A. Nyakatura, A. Jusufi, Inertial Tail Effects during Righting of Squirrels in Unexpected Falls: From Behavior to Robotics, *Integr. Comp. Biol.* 61 (2) (2021) 589–602.
- [14] Y.-H. Lin, R. Siddall, F. Schwab, T. Fukushima, H. Banerjee, Y. Baek, D. Vogt, Y.-L. Park, A. Jusufi, Modeling and Control of a Soft Robotic Fish with Integrated Soft Sensing, *Adv. Intell. Syst.* (2021) 2000244, <https://doi.org/10.1002/aisy.202000244>.
- [15] Z. Song, J. Tong, W. Pfleging, J. Sun, A review: Learning from the flight of beetles, *Comput. Biol. Med.* 133 (2021) 104397, <https://doi.org/10.1016/j.combiomed.2021.104397>.
- [16] K. Saito, S. Nomura, S. Yamamoto, R. Niiyama, Y. Okabe, Investigation of hindwing folding in ladybird beetles by artificial elytron transplantation and microcomputed tomography, *Proc. Natl. Acad. Sci.* 114 (22) (2017) 5624–5628.
- [17] G. Pass, Beyond aerodynamics: The critical roles of the circulatory and tracheal systems in maintaining insect wing functionality, *Arthropod Structure & Development* 47 (4) (2018) 391–407.
- [18] J. Sun, M. Ling, W. Wu, B. Bhushan, J. Tong, The Hydraulic Mechanism of the Unfolding of Hind Wings in *Dorcus titanus platymelus* (Order: Coleoptera), *Int. J. Mol. Sci.* 15 (4) (2014) 6009–6018.
- [19] J.Y. Sun, W. Wu, M.Z. Ling, B. Bhushan, J. Tong, The hydraulic mechanism in the hind wing veins of *Cybister japonicus* Sharp (order: Coleoptera), *Beilstein J. Nanotechnol.* 7 (2016) 904–913.

- [20] T. Geisler, Observations and Measurements of Wing Parameters of the Selected Beetle Species and the Design of a Mechanism Structure Implementing a Complex Wing Movement, *International Journal of Applied Mechanics and Engineering* 21 (4) (2016) 837–847.
- [21] S. Shield, R. Jericevich, A. Patel, A. Jusufi, Tails, Flails, and Sails: How Appendages Improve Terrestrial Maneuverability by Improving Stability, *Integr. Comp. Biol.* 61 (2) (2021) 506–520.
- [22] C. Kropf, Hydraulic System of Locomotion, in: W. Nentwig (Ed.), *Spider Ecophysiology*, Springer, Berlin Heidelberg, 2013, pp. 43–56.
- [23] P. Polygerinos, N. Correll, S.A. Morin, B. Mosadegh, C.D. Onal, K. Petersen, M. Cianchetti, M.T. Tolley, R.F. Shepherd, Soft Robotics: Review of Fluid-Driven Intrinsically Soft Devices; Manufacturing, Sensing, Control, and Applications in Human-Robot Interaction, Control, and Applications in Human-Robot Interaction *Advanced Engineering Materials* 19 (12) (2017) 1700016, <https://doi.org/10.1002/adem.201700016>.
- [24] F. Schwab, F. Wiesemüller, C. Mucignat, Y.-L. Park, I. Lunati, M. Kovac, A. Jusufi, Undulatory Swimming Performance Explored With a Biorobotic Fish and Measured by Soft Sensors and Particle Image Velocimetry, *Frontiers in Robotics and AI* 8 (2022).
- [25] T.H. Yang, J. Shintake, R. Kanno, C.R. Kao, J. Mizuno, Low-Cost Sensor-Rich Fluidic Elastomer Actuators Embedded with Paper Electronics, *Advanced Intelligent Systems* 2 (8) (2020) 2000025, <https://doi.org/10.1002/aisy.202000025>.
- [26] R. Hufenus, Y. Yan, M. Dauner, T. Kikutani, Melt-Spun Fibers for Textile Applications, *Materials* 13 (19) (2020) 4298, <https://doi.org/10.3390/ma13194298>.
- [27] R. Hufenus, Y. Yan, M. Dauner, D. Yao, T. Kikutani, Bicomponent Fibers, in: J. Hu, B. Kumar, J. Lu (Eds.), *Handbook of Fibrous Materials*, vol. 1, Wiley-VCH, Weinheim, 2020, pp. 281–313.
- [28] R. Hufenus, L. Gottardo, A.A. Leal, A. Zemp, K. Heutschi, P. Schuetz, V.R. Meyer, M. Heuberger, Melt-spun polymer fibers with liquid core exhibit enhanced mechanical damping, *Mater. Des.* 110 (2016) 685–692.
- [29] S. Kling, T. Czizgany, Damage detection and self-repair in hollow glass fiber fabric-reinforced epoxy composites via fiber filling, *Compos. Sci. Technol.* 99 (2014) 82–88.
- [30] M.-U. Saeed, ZhaoFeng Chen, BinBin Li, Manufacturing strategies for microvascular polymeric composites: A review, *Compos. A Appl. Sci. Manuf.* 78 (2015) 327–340.
- [31] Y. Zhu, X.J. Ye, M.Z. Rong, M.Q. Zhang, Self-healing glass fiber/epoxy composites with polypropylene tubes containing self-pressurized epoxy and mercaptan healing agents, *Compos. Sci. Technol.* 135 (2016) 146–152.
- [32] C. Wang, L. Zeng, Z. Li, D. Li, Review of optical fibre probes for enhanced Raman sensing, *J. Raman Spectrosc.* 48 (8) (2017) 1040–1055.
- [33] M. Chemnitz, M. Gebhardt, C. Gaida, F. Stutzki, J. Kobelke, J. Limpert, A. Tünnermann, M.A. Schmidt, Hybrid soliton dynamics in liquid-core fibres, *Nat. Commun.* 8 (1) (2017) 42.
- [34] A.A. Leal, M. Naeimirad, L. Gottardo, P. Schuetz, A. Zadhouh, R. Hufenus, Microfluidic behavior in melt-spun hollow and liquid core fibers, *Int. J. Polym. Mater.* 65 (9) (2016) 451–456.
- [35] M. Naeimirad, A. Zadhouh, A. Abrishamkar, A. Pishevar, A.A. Leal, Melt-spun liquid core fibers: physical and morphological characteristics, *Iran. Polym. J.* 25 (5) (2016) 397–403, <https://doi.org/10.1007/s13726-016-0431-y>.
- [36] Kirby B. Micro-, and Nanoscale Fluid Mechanics: Transport in Microfluidic Devices, Cambridge University Press, 2010.
- [37] L.G.M. Pettersson, R.H. Henchman, A. Nilsson, Water—The Most Anomalous Liquid, *Chem. Rev.* 116 (13) (2016) 7459–7462.
- [38] W. Fritz, Bemerkungen zum Auslaufbecher DIN 53211, *Chem. Ing. Tech.* 21 (5–6) (1949) 103–105.
- [39] F.A. Reifler, R. Hufenus, M. Krehel, E. Zraggen, R.M. Rossi, L.J. Scherer, Polymer optical fibers for textile applications – Bicomponent melt spinning from cyclic olefin polymer and structural characteristics revealed by wide angle X-ray diffraction, *Polymer* 55 (22) (2014) 5695–5707.
- [40] Dow Chemical, <https://www.dow.com/en-us/pdp/versify-4200-plastomer.108441z.html> (accessed June 10, 2022).
- [41] F. Selli, U.H. Erdoğan, R. Hufenus, E. Perret, Mesophase in melt-spun poly( $\epsilon$ -caprolactone) filaments: Structure–mechanical property relationship, *Polymer* 206 (2020) 122870, <https://doi.org/10.1016/j.polymer.2020.122870>.
- [42] K. Jakubowski, C.-S. Huang, A. Gooneie, L.F. Boesel, M. Heuberger, R. Hufenus, Luminescent solar concentrators based on melt-spun polymer optical fibers, *Mater. Des.* 189 (2020) 108518, <https://doi.org/10.1016/j.matdes.2020.108518>.
- [43] OpenFOAM, <https://openfoam.org> (accessed June 10, 2022).
- [44] F. Moukalled, L. Mangani, M. Darwish, *The Finite Volume Method in Computational Fluid Dynamics*, Springer International Publishing, Switzerland, 2016.
- [45] M. Nekouei, S.A. Vanapalli, Volume-of-fluid simulations in microfluidic T-junction devices: Influence of viscosity ratio on droplet size, *Phys. Fluids* 29 (3) (2017) 032007, <https://doi.org/10.1063/1.4978801>.
- [46] J.K. Nunes, S.S.H. Tsai, J. Wan, H.A. Stone, Dripping and jetting in microfluidic multiphase flows applied to particle and fibre synthesis, *J. Phys. D Appl. Phys.* 46 (11) (2013) 114002, <https://doi.org/10.1088/0022-3727/46/11/114002>.
- [47] P. Simonetti, R. Nazir, A. Gooneie, S. Lehner, M. Jovic, K.A. Salmeia, R. Hufenus, A. Rippl, J.-P. Kaiser, C. Hirsch, B. Rubi, S. Gaan, Michael addition in reactive extrusion: A facile sustainable route to developing phosphorus based flame retardant materials, *Compos. B Eng.* 178 (2019) 107470, <https://doi.org/10.1016/j.compositesb.2019.107470>.
- [48] C. Bascucci, I. Duretek, S. Lehner, C. Holzer, S. Gaan, R. Hufenus, A. Gooneie, Investigating thermomechanical recycling of poly(ethylene terephthalate) containing phosphorus flame retardants, *Polymer Degradation and Stability* 195 (2022) 109783, <https://doi.org/10.1016/j.polymdegradstab.2021.109783>.
- [49] A. Gooneie, P. Simonetti, P. Rupper, R. Nazir, M. Jovic, S. Gaan, M.P. Heuberger, R. Hufenus, Stabilizing effects of novel phosphorus flame retardant on PET for high-temperature applications, *Mater. Lett.* 276 (2020) 128225, <https://doi.org/10.1016/j.matlet.2020.128225>.
- [50] C. Tréguët, A. Mikhailovskaya, T. Salez, N. Pantoustier, P. Perrin, M. Reyssat, C. Monteux, Adsorption dynamics of hydrophobically modified polymers at an air-water interface, *The European Physical Journal E* 41 (9) (2018) 101.
- [51] G. Wu, S. Sun, X. Zhu, Z. Ma, Y. Zhang, N. Bao, Microfluidic Fabrication of Hierarchical-Ordered ZIF-L(Zn)/Ti3C2Tx Core-Sheath Fibers for High-Performance Asymmetric Supercapacitors, *Angew. Chem. Int. Ed.* 61 (8) (2022), <https://doi.org/10.1002/anie.202115559>.
- [52] M.A. Herrada, A.M. Gañán-Calvo, P. Guillot, Spatiotemporal instability of a confined capillary jet, *Phys. Rev. E* 78 (4) (2008) 046312.
- [53] Y. Kou, S. Wang, J. Luo, K. Sun, J. Zhang, Z. Tan, Q. Shi, Thermal analysis and heat capacity study of polyethylene glycol (PEG) phase change materials for thermal energy storage applications, *J. Chem. Thermodyn.* 128 (2019) 259–274.
- [54] Y. Yan, W. Li, R. Zhu, C. Lin, R. Hufenus, Flexible Phase Change Material Fiber: A Simple Route to Thermal Energy Control Textiles, *Materials* 14 (2) (2021) 401.
- [55] K. Jakubowski, W. Kerkemeyer, E. Perret, M. Heuberger, R. Hufenus, Liquid-core polymer optical fibers for luminescent waveguide applications, *Mater. Des.* 196 (2020) 109131, <https://doi.org/10.1016/j.matdes.2020.109131>.
- [56] R.K. Roeder, Chapter 3 – Mechanical Characterization of Biomaterials, in: A. Bandyopadhyay, S. Bose (Eds.), *Characterization of Biomaterials*, Academic Press, Oxford, 2013, pp. 49–104.
- [57] C. Suchocki, R. Molak, On relevance of time-dependent Poisson's ratio for determination of relaxation function parameters, *J. Braz. Soc. Mech. Sci. Eng.* 41 (11) (2019) 519.
- [58] M. Chellapurath, P. Khandelwal, T. Rottier, F. Schwab, A. Jusufi, Morphologically Adaptive Crash Landing on a Wall: Soft-Bodied Models of Gliding Geckos with Varying Material Stiffnesses, *Advanced Intelligent Systems* (2022) 2200120, <https://doi.org/10.1002/aisy.202200120>.
- [59] R. Baines, S. Freeman, F. Fish, R. Kramer-Bottiglio, Variable stiffness morphing limb for amphibious legged robots inspired by chelonian environmental adaptations, *Bioinspiration Biomimetics* 15 (2) (2020) 025002, <https://doi.org/10.1088/1748-3190/ab68e8>.
- [60] B. McInroe, H.C. Astley, C. Gong, S.M. Kawano, P.E. Schiebel, J.M. Rieser, H. Choset, R.W. Blob, D.I. Goldman, Tail use improves performance on soft substrates in models of early vertebrate land locomotors, *Science* 353 (6295) (2016) 154–158.
- [61] R. Siddall, V. Ibanez, G. Byrnes, R.J. Full, A. Jusufi, Mechanisms for Mid-Air Reorientation Using Tail Rotation in Gliding Geckos, *Integr. Comp. Biol.* 61 (2) (2021) 478–490.